

Article

Ionic Mobility and Phase Transitions in Perovskite Oxides for Energy Applications

Francesco Cordero ^{1,*}, Floriana Craciun ¹ and Francesco Trequattrini ^{2,3}

¹ CNR-ISC, Istituto dei Sistemi Complessi, Area della Ricerca di Roma - Tor Vergata, Via del Fosso del Cavaliere 100, I-00133 Roma, Italy; floriana.craciun@isc.cnr.it

² Dipartimento di Fisica, Università di Roma La Sapienza, P.le A. Moro 2, I-00185 Roma, Italy; francesco.trequattrini@roma1.infn.it

³ Consiglio Nazionale delle Ricerche, Istituto dei Sistemi Complessi, U.O.S. La Sapienza, Piazzale A. Moro 5, 00185 Roma, Italy

* Correspondence: francesco.cordero@isc.cnr.it; Tel.: +39-06-4993-4114

Academic Editor: Palmiro Poltronieri

Received: 30 December 2016; Accepted: 7 February 2017; Published: 13 February 2017

Abstract: Perovskite oxides find applications or are studied in many fields related to energy production, accumulation and saving. The most obvious application is oxygen or proton conductors in fuel cells (SOFCs), but the (anti)ferroelectric compositions may find application in high energy capacitors for energy storage, efficient electrocaloric cooling, and electromechanical energy harvesting. In SOFCs, the diffusion of O vacancies and other mobile ionic species, such as H⁺, are at the base of the functioning of the device, while in the other cases they constitute unwanted defects that reduce the performance and life-time of the device. Similarly, the (anti)ferroelectric phase transitions are a requisite for the use of some types of devices, but the accompanying domain walls can generate extended defects detrimental to the life of the material, and structural phase transformations should be avoided in SOFCs. All these phenomena can be studied by mechanical spectroscopy, the measurement of the complex elastic compliance as a function of temperature and frequency, which is the mechanical analogue of the dielectric susceptibility, but probes the elastic response and elastic dipoles instead of the dielectric response and electric dipoles. The two techniques can be combined to provide a comprehensive picture of the material properties. Examples are shown of the study of structural transitions and hopping and tunneling processes of O vacancies and H in the ion conductor BaCe_{1-x}Y_xO_{3-x} and in SrTiO_{3-x}, and of the aging and fatigue effects found in PZT at compositions where the ferro- and antiferroelectric states coexist.

Keywords: perovskites; ferroelectrics; ionic conductors; O vacancies; defects mobility and clustering; anelastic relaxation; dielectric relaxation; PZT; strontium titanate

1. Introduction

Perovskite oxides find applications or are studied in many fields related to energy production, accumulation and saving. Examples are the oxygen and proton conductors as solid electrolytes for fuel cells (SOFCs) [1], and the ferroelectric (FE) and antiferroelectric (AFE) compositions, which may find application in high energy capacitors for energy storage [2,3], efficient electrocaloric cooling [4], and electromechanical energy harvesting [5]. Figure 1 presents the cell of a cubic perovskite ABO₃ and ranges of different properties depending on the choice of the A and B cations. When the $-6e$ charge of the ideally three O²⁻ atoms per unit cell is not fully compensated by the cation valence $\langle v_A \rangle + \langle v_B \rangle$, then V_O are created and this can be exploited for creating a fast ion conductor. In fact O is the most mobile atomic species in a perovskite, but cannot occupy interstitial positions, due to the compactness of the perovskite structure; in addition, by exposure to humid atmosphere at moderately

high temperature it is possible to fill a V_O with an $(OH)^-$ hydroxide ion obtaining a proton conductor. A typical superionic conductor is $BaCe_{1-x}Y_xO_{3-x/2}$, but recently it has been found that also FE perovskites like $Na_{1/2}Bi_{1/2}TiO_3$ (NBT) can be made superionic conductors by doping, for example, with Mg [6].

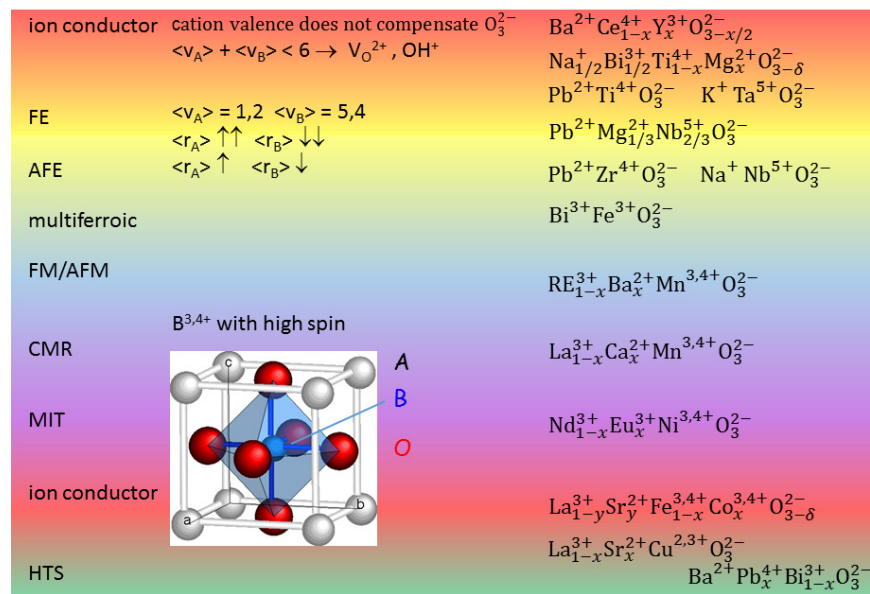


Figure 1. The cubic perovskite structure and some types of perovskites exhibiting different properties; v indicates the valence and r is the ionic radius.

Figure 1 shows that FE phases can be obtained when the A cations have large size and low valence and B small size and large valence. A simple explanation for this fact is that the small B ion may go off-centre in the large O_6^{2-} octahedron and produce an electric dipole with its large positive charge, though additional mechanisms are also important [7,8]. By decreasing the size mismatch between A and B, it is possible to stabilize also AFE phases, as in Zr-rich PZT. It has been discussed how the main source of magnetism, namely partially filled d or f orbitals, is in contrast with the common source of FE, a small B cation with empty d and f shells [9]; nonetheless, there are various mechanisms leading to FE, and hence various types of perovskites exhibiting both FE and magnetism, the so-called multiferroics [9]. Perovskites with $B = Mn, Ni$, which cause Jahn-Teller distortions of the BO_6 octahedra, exhibit other phenomena like charge and orbital ordering, metal/insulator transitions and colossal magnetoresistance [7], and turning back the focus on the materials for energy applications, good ionic conductors are found with $B = Fe, Co$ [10].

In SOFCs, the fast diffusion of O vacancies (V_O), protons and other mobile ionic species are exploited in order to produce an electronic current in the external circuit at the expense of the chemical energy in the fuel, while the structural phase transitions should be avoided or tuned in such a manner to minimize their negative effects on the ionic mobilities and as sources of mechanical failure. On the other hand, in the applications based on the FE/AFE states, the FE properties and the FE/AFE transitions have to be optimized and tuned in order to maximize the stored electric energy, and electrocaloric and piezoelectric coefficients, while the V_O and other mobile ionic species constitute unwanted defects that reduce the performance and life-time of the device.

It is therefore clear that in all these cases it is important, though for different reasons, to understand and control the phase transformations and ions mobilities, ordering or clustering. All these phenomena can be studied by anelastic (or mechanical) spectroscopy, the measurement of the complex compliance as a function of temperature and frequency. It is the mechanical analogue of the dielectric susceptibility,

and probes the elastic response and dipoles instead of the dielectric response and electric dipoles. The two techniques are complementary, and can provide a comprehensive picture of the materials properties. Examples are shown of the study the mobility and clustering of V_O in $SrTiO_3$, a model perovskite with a simple cubic structure, then of structural transitions and hopping and tunneling of V_O and H in the ion conductor $BaCe_{1-x}Y_xO_{3-\delta}$, and finally of the aging and fatigue effects found in $PbZr_{1-x}Ti_xO_3$ (PZT) at compositions where the FE and AFE states coexist.

2. Materials and Methods

The ceramic $SrTiO_3$ samples were prepared by solid state reaction for 6 h at 1100 °C, followed by sintering in air at 1450 °C, as described in Ref. [11]. The ingots had a relative density of 97% and were cut as thin bars $45 \times 5 \times 0.5 \text{ mm}^3$ for the anelastic experiments. The $SrTiO_3$ single crystal was cut from a wafer from M.T.I. Corporation as a bar of $26 \times 3.4 \times 0.5 \text{ mm}^3$, with the edges parallel to the (100) directions. The reduction and reoxygenation treatments were made either in static H_2 or O_2 atmosphere in a quartz tube connected to a UHV system and heated by a tubular furnace to 1000–1150 °C, or in a flux of $0.1CO + 0.9Ar$ or O_2 gas within a quartz tube with water cooled jacket and heated by induction by an external coil. In the latter case, the sample was contained in a Pt enclosure that could be heated by induction. The amount of O absorbed or lost was checked by the mass change before and after the treatment.

The electrolytes for fuel cells were $BaCe_{1-x}Y_xO_3$ with $x \leq 0.15$ prepared from powders obtained by auto-combustion synthesis, crystallized in air at 1000 °C for 5 as described in Ref. [12]. No impurity phases were detected by X-ray diffraction (XRD). The powders were uniaxially pressed at 50 MPa and then isostatically pressed at 200 MPa into $60 \times 7 \times 6 \text{ mm}^3$ ingots, which were sintered at 1500 °C for 10 h and cut as thin bars about 1 mm thick and ~ 40 mm long, optimal for the anelastic experiments. In order to hydrate the samples, they were kept for 1–2 h at 793 K in a static atmosphere of 50–100 mbar H_2O or D_2O , while outgassing was obtained in a vacuum of $<10^{-5}$ mbar up to 730 °C or during the anelastic experiments. The resulting variations of the gaseous contents were monitored from the change of weight.

The PZT samples were prepared by solid state reaction with calcination at 700 °C for 4 h, pressing into bars, sintering at 1250 °C for 2 h together with $PbZrO_3 + 5 \text{ wt } \% \text{ excess } ZrO_2$ powder to prevent PbO loss to obtain ingots with 95% of the theoretical density and large grains, 5–20 μm , as described in Ref. [13].

In all cases it was checked by XRD that no impurity phases were present after calcination and sintering. All the samples were finally cut as thin (0.5–1 mm) bars with lengths between 25 and 45 mm for the anelastic experiments. When also dielectric measurements were done, to both major faces were applied electrodes with Ag paint, otherwise only to one face or its center and edge, in order to assist the electrostatic excitation and for shorting the thermocouple wires.

The elastic compliance $s(\omega, T) = s' - is''$, the reciprocal of Young's modulus E , was measured by electrostatically exciting the flexural modes of the bars suspended in vacuum on thin thermocouple wires in correspondence with the nodal lines; technique and apparatus are described in Ref. [14], and for a general treatment of anelasticity see Ref. [15]. In these conditions, during the same run it is possible to measure the 1st, 3rd and 5th modes, whose frequencies are in the ratios 1:5.4:13.3, and the fundamental frequencies are in the range $\omega/2\pi \simeq 1\text{--}5 \text{ kHz}$, depending on the sample shape and state. The data are presented as real part s' of the elastic compliance $s(\omega, T) = s' - is'' = E^{-1}$, referred to its extrapolation s_0 to 0 K or in the paraelectric phase, and elastic energy loss $Q^{-1} = s''/s'$. The first is proportional to the square of the sample resonance frequency, $s'(T) \propto 1/\omega^2(T)$, and presents peaks or steps at the structural phase transformations; the latter is measured from the decay of the free oscillations or from the width of the resonance peak, and presents peaks due to the relaxational motion of point and extended defects [15], as described by Equation (2) later on.

The dielectric permittivity $\epsilon = \epsilon' - i\epsilon''$ of small discs with 11 mm of diameter and ~ 1 mm thick was measured with a HP 4284A impedance bridge with a four wire probe between 100 Hz and

100 kHz in a modified Linkam HFS600E-PB4 stage. For the dielectric measurements of Figure 6 the same samples and cryostat for the anelastic measurements were used. After depositing the Ag electrodes, an intense dielectric relaxation process, identified with the motion of charge carriers within a Schottky barrier at the electrode interface, completely masked the true bulk relaxation. The effect was suppressed by applying 40 V up to ~ 500 K, switching the direction of the dc current in order to avoid electromigration of O vacancies or protons [12].

3. Oxygen Vacancy and Proton Mobilities and Aggregations in Ionic Conductors

The ionic transport in solids is often characterized in terms of an overall diffusion coefficient, for example, by means of chemical or tracer diffusion experiments, useful for example in the choice of a solid electrolyte for fuel cells. Yet, such a description is far from complete when the diffusion process is composed of several steps with very different characteristic times. For example, the fastest ion present in any oxide is O, which in perovskites cannot find space in interstitial position, and therefore diffuses via an O vacancy (V_O). Oxygen vacancies may be trapped by acceptor defects or can form stable pairs or larger complexes; therefore, the long range migration consists of a sequence of dissociation of the V_O from a defect complex, fast diffusion and retrapping at another defect complex. The individual steps of the ionic migration are experimentally accessible through the dielectric, anelastic and NMR spectroscopies, since they produce peaks at their distinct characteristic frequencies in the respective susceptibilities [16]. Therefore, a particular hopping, reorientation or association/dissociation process occurring with characteristic time τ between two states with relative populations n_1 and n_2 will produce a Debye peak in the imaginary part of the dielectric susceptibility ϵ'' , elastic compliance s'' or Nuclear Quadrupolar Relaxation (NQR) rate W_Q

$$\epsilon'' = \frac{4n_1n_2}{k_B T} c v_0 (\Delta p)^2 \frac{\omega\tau}{1 + (\omega\tau)^2} \quad (1)$$

$$s'' = \frac{4n_1n_2}{k_B T} c v_0 (\Delta\lambda)^2 \frac{\omega\tau}{1 + (\omega\tau)^2} \quad (2)$$

$$W_Q \propto \frac{n_1n_2}{k_B T} c \frac{\omega\tau}{1 + (\omega\tau)^2} \quad (3)$$

where ω is the measuring angular frequency, c the molar concentration of defects, v_0 the molecular volume, Δp and $\Delta\lambda$ denote the changes in electric and elastic dipoles during the elementary process. Since the hopping/reorientation time τ usually follows the Arrhenius law

$$\tau = \tau_0 \exp(E/k_B T) \quad (4)$$

where E is the potential barrier or activation energy, the imaginary susceptibilities versus T exhibit maxima at the temperatures T_M where the condition

$$\omega\tau(T_M) \simeq 1 \quad (5)$$

are verified for a particular elementary process. The above formulas are valid for noninteracting point defects and, depending whether they possess an elastic and/or dielectric dipole that can reorient or change or a nuclear quadrupolar moment that feels a varying crystalline field, one can observe one or more of the above relaxations. The relaxation times τ of the three types of relaxations may differ of factors of order 2, due to the different numbers of non equivalent elastic/dielectric dipole configurations (see e.g., [15] p. 306). At high concentrations, the point defects interact with each other, causing important deviations from the above picture, which can be taken into account in various manners: for example, introducing various types of distributions of relaxation times [15], by introducing interactions of local type in the partition function of the defects [17], in the mean field

approximation deriving divergences of the relaxation time and strength of the Curie-Weiss type [18] or in the Bragg-Williams scheme [19,20].

The NQR experiments require rather substantial an equipment and analysis and are seldom used for similar purposes [16,21], while anelastic relaxation experiments are more usual and dielectric susceptibility or impedance spectroscopy are commonly used. A combination of the latter is very useful, since the dielectric susceptibility probes the reorientation of electric dipoles and long range charge diffusion, including the charge carriers, while the elastic compliance only probes ionic and polaronic motions producing changes in strain; therefore is insensitive to the motion of free carriers and gives a clean picture of the ionic motions, also in the presence of electronic conductivity.

3.1. Mobility and Clustering of V_O in the Simplest Case: Cubic $SrTiO_3$

An ideal starting point for the study of V_O in perovskites is $SrTiO_{3-\delta}$, which has been continuously studied in the O deficient state since the 1960's in various contexts, from superconductivity to ion conduction, and is one of the few perovskites that remains cubic down to low temperature. The commonplace has been for a long time that in $SrTiO_3$, and hence in perovskite titanates, the V_O are uniformly distributed up to concentrations of several molar percent and diffuse with an activation energy whose value varies much among different studies [22], but the consensus was for a barrier of 1–1.2 eV (see e.g., [23,24]). When faster diffusion was estimated, it was attributed to the presence of dislocations acting as channels for easy diffusion [23]. An NMR experiment convincingly showing that the barrier for V_O hopping is 0.63 eV in Fe-doped $SrTiO_3$ [21] passed unobserved, but recently attention started to be paid to V_O clustering, especially in the near surface regions [25].

The bias for 1 eV as the typical barrier for O diffusion in perovskite titanates induced also us to initially wrongly interpret the anelastic spectrum of reduced $SrTiO_3$ [11]. Figure 2 shows that the elastic energy loss measured at kHz on ceramic $SrTiO_3$ reduced at 1100 °C in H_2 atmosphere presents three peaks above room temperature, labelled P1 to P3 starting from high temperature. From the temperature shifts observed during the same run at higher frequency, it was deduced that the activation energies are 1 eV for P1 and 0.6 eV for P3 (see Equations (4) and (5)); therefore P1 was assigned to the jumps of the V_O , in accordance with the prevalent opinion, and P3 to H introduced during the treatment in H_2 atmosphere [11]. We then repeated the experiments using CO as reducing agent, in order to avoid the possible introduction of unwanted H, and the surprising result was that the anelastic spectrum was identical. This is shown in Figure 2 for a similar ceramic sample reduced for 3 h at 1100 °C in a flux of 0.9Ar + 0.1CO (empty symbols). The same figure shows also the anelastic spectra of a single crystal in the virgin state and after reduction in CO flux, with $\delta = 0.0049$, as deduced from the mass variation after reduction and subsequent reoxygenation and from the shift of the temperature of the structural transition at 105 K [26]. The shift to higher temperature of the peaks in the crystal is due to the higher frequency of measurement (5 kHz, see the condition (5) for the peak maxima), while the difference in their relative intensities, especially the reduction of P2, is due to the fact that in the ceramic samples all the components of the elastic compliance are probed, while in the crystal only s_{11} was probed.

The evolution of the anelastic spectrum with increasing δ is shown in Figure 3: initially only P3 is observed, but its height saturates soon after the appearance of P1, which then becomes dominant. Also the additional peaks P5 and P6 appear at lower temperatures, and are probably due to hopping of polarons. Instead, the set of P1, P2 and P3 peaks can be perfectly fitted assuming that P3 is due to isolated V_O , while P1 is due to the full process of reorientation of V_O pairs, and P2 is due to the intermediate dissociation step necessary for the pair reorientation [26]. The right hand side of Figure 3 also shows the dependence on temperature of the peak intensities, deduced from the spectrum shifted at higher temperature when measured at higher frequency. The intensity of P3 is $\propto 1/T$ at low δ , as expected from all V_O being isolated and hopping between equivalent states (Equation (2) with $c = \text{const}$ and $n_1 = n_2 = 1/2$), but increases with T at higher δ , consistent with the fact that at

higher δ there is a fraction of V_O that are paired or aggregated and become isolated with increasing T . Accordingly, the intensity of P1 decreases faster than $1/T$.

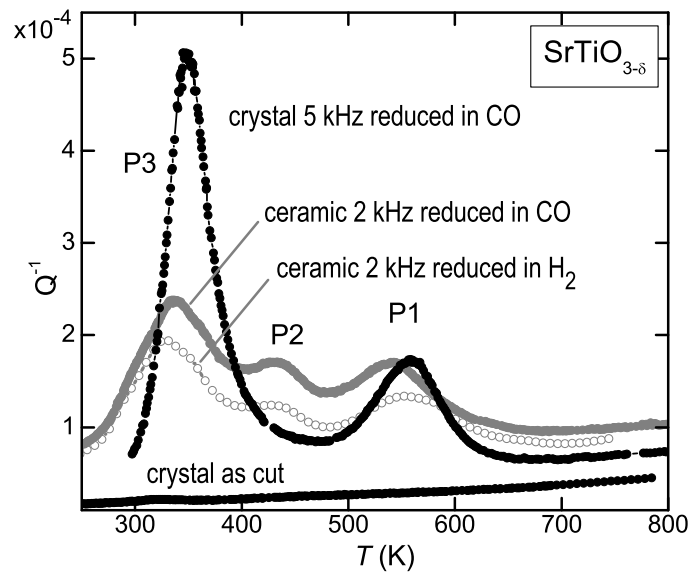


Figure 2. Elastic energy loss, Q^{-1} , of ceramic and single crystal $SrTiO_{3-\delta}$ in the virgin state and after reduction in CO or H_2 atmosphere.

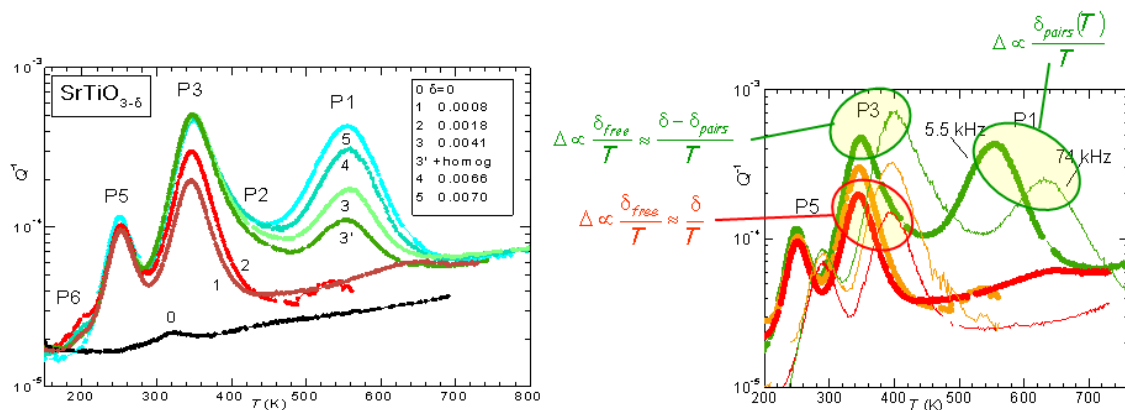


Figure 3. Elastic energy loss, Q^{-1} , of single crystal $SrTiO_{3-\delta}$ at various levels of O deficiency measured at 5.5 kHz. Right side: $Q^{-1}(T)$ curves measured at 5.5 and 74 kHz for $\delta = 0.0008, 0.0018$ and 0.0070 . Adapted with permission from Ref. [26], copyrighted by the American Physical Society.

All this has been quantitatively verified by fitting with the same set of parameters many different $Q^{-1}(T)$ curves at various frequencies and values of δ , though with approximate expressions for the pairs and clusters populations [26]. An example is presented in Figure 4. The jump rate of the isolated V_O (peak P3) follows Equation (4) with $\tau_{03} = 5 \times 10^{-14}$ s, $E_3 = 0.60$ eV, while the pair reorientation rate (peak P1) has $\tau_{01} = 7 \times 10^{-14}$ s, $E_1 = 0.97$ eV. The binding energies are estimated as $E_{bp} = 0.18$ eV for V_O pairs or ends of longer chains, and $E_{bc} = 0.26$ eV for the chains. The intensity of P2 is smaller than that of P1 and P3 because it is due to a relaxation mode between bound and unbound states, which differ in energy of E_{bp} ; since $E_{bp}/k_B \sim 2000$ K, the population of the unbound state is much smaller than that of the bound state, i.e., $n_2 \ll n_1$ in Equation (2) and therefore $n_1 n_2 \ll 1$, whereas in the other cases $n_1 \simeq n_2 \simeq 1/2$.

From the fact that $E_3 - E_1 > E_{bp}, E_{bc}$ it follows that the saddle points between dissociated and paired or clustered configurations of V_O are higher than for isolated V_O , and this may be a

consequence of the electrostatic repulsion between V_O . A similar observation had been done for the mobile non-stoichiometric O atoms in the $\text{CuO}_{2-\delta}$ planes of $\text{YBa}_2\text{Cu}_3\text{O}_{7-\delta}$ [27], and has the consequence that the time for reaching equilibrium is longer than expected from the fast diffusion of isolated V_O or O atoms: they approach to each other at a fast rate, but have to win the electrostatic repulsion in order to form the bound state.

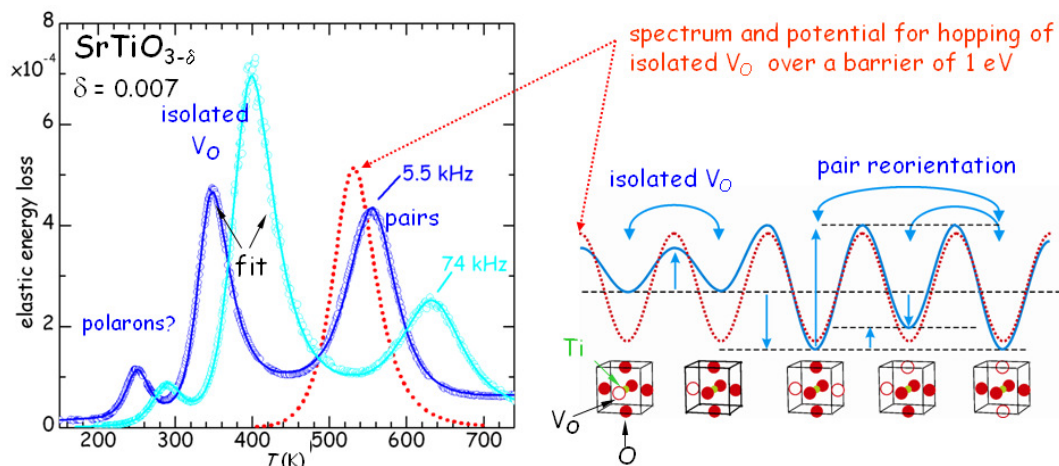


Figure 4. Left: anelastic spectrum of $\text{SrTiO}_{3-\delta}$ with $\delta = 0.007$ measured at 5.5 and 74 kHz and fit assuming contributions from the V_O configurations represented in the right side with the blue potential. The dashed red peak on the left would be the anelastic spectrum from isolated V_O hopping over a barrier of 1 eV (dashed red potential). Adapted with permission from Ref. [26], copyrighted by the American Physical Society.

These anelastic experiments show that, even at high dilution, well below 1%, the V_O behave in quite a non trivial manner also in the bulk of undoped cubic $\text{SrTiO}_{3-\delta}$. Therefore, the interpretation of experiments probing an overall mobility in terms of an activation enthalpy for diffusion of isolated V_O is wrong; what is probed is, in fact, the rate limiting step of the association/dissociation processes, peak P1 in the above anelastic spectra, which in fact has the same activation energy of 1 eV generally assumed for V_O diffusion. The other experimental technique from which information on the detailed microscopic mechanisms of V_O mobility and clustering can be obtained is NQR relaxation [16,21], while dielectric experiments are of limited utility in the case of isolated V_O , which do not possess an electric dipole.

3.2. Mobility and Clustering of V_O and H in $\text{BaCe}_{1-x}\text{Y}_x\text{O}_3$

Some results are described now of combined anelastic and dielectric studies of $\text{BaCe}_{1-x}\text{Y}_x\text{O}_{3-\delta}\text{H}_y$ (BCY100x) used as solid state electrode in SOFCs. Hydration is obtained by exposing the as prepared material, which has $\delta \simeq x/2$ for compensating the unbalanced charge of $x \text{Ce}^{4+}$ substituted by Y^{3+} with $x/2 V_O$, where the two dots indicate that an V_O has charge $+2e$ with respect to a regular O^{2-} . The V_O can be filled with $(\text{OH})^-$ hydroxide ions by exposure to humid atmosphere at high temperature, rendering the material a proton conductor, and the whole range of hydration levels, from complete with $\delta = 0$ and $y = x/2$ to outgassed with $\delta = x/2$, $y = 0$, is in principle accessible by varying the H_2O partial pressure. Figure 5a presents the anelastic spectrum of BCY15 in the hydrated state.

It is easy to distinguish the thermally activated processes of ionic hopping (RH and R6), which shift to higher T when measured at higher f , from the structural transformations, which appear as steps or maxima in the compliance at temperatures independent of f (PT1 and PT2). Indications on the nature of the various microscopic processes can be obtained from the evolution of the anelastic spectrum when passing from the outgassed to the hydrated state, as shown in Figure 5b.

In this manner it also appears that there are several thermally activated peaks from low to room temperature, labelled R1, R2, R3 and RH. All of them have an intensity that increases with the level of hydration, and therefore are to be attributed directly to the motion of protons or to small polarons associated with H. On the other hand, peaks RV and R6 are absent in the hydrated state and fully developed in the outgassed state, and therefore are clearly due to V_O . A full analysis of the complex anelastic spectra has not been attempted yet, but it is reasonable to assume that RH and R3 are due to proton hopping among different O atoms near a trapping Y^{3+} acceptor and far from it, while R6 and RV are due to hopping of V_O in the trapped and free state [12,28]. That V_O and H are trapped by acceptor impurities is understandable from simple considerations of electrostatic attraction, and confirmed both experimentally [29] and by first principle calculations [30].

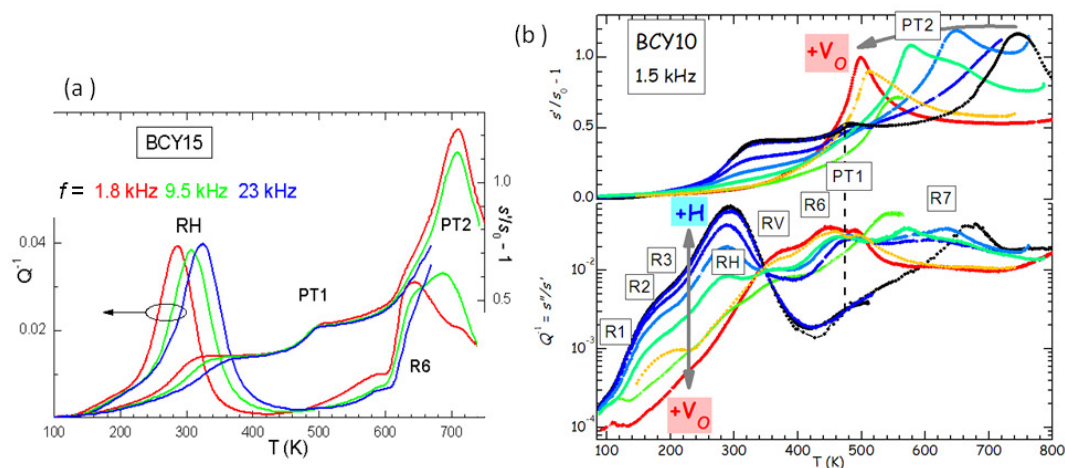


Figure 5. (a) Elastic energy loss and compliance s' normalized to its value s_0 at 0 K of hydrated $BaCe_{1-x}Y_xO_3$ with $x = 0.15$, measured during the same run at three frequencies; (b) Elastic energy loss and normalized compliance of $BaCe_{1-x}Y_xO_3$ with $x = 0.10$ at different levels of hydration and outgassing. The thermally activated relaxation processes are labelled as R_x , while the phase transitions with PT_x . The arrows indicate the sequence according to increasing hydration (+H) or outgassing (+ V_O).

The phenomenon of trapping is generally unwanted in a superionic conductor, because it reduces the ionic mobility, but it is also unavoidable, since, as we have seen with $SrTiO_3$ in the previous section, in the absence of acceptor dopants there is need of an extremely reducing environment in order to introduce a sizeable amount of V_O , and H is hardly absorbed. Yet, the complicated phenomena occurring in the presence of high concentrations of both V_O and H may also suggest strategies for improving the ionic mobilities. For example, the reciprocal repulsion of V_O^+ and H^+ prevents H trapping at dopants already associated with an V_O , which should increase the proton mobility [31].

The diffusion of H in a perovskite ABO_3 is actually more complicated than simple hopping between O atoms, because it includes a fast tunnel assisted motion around the B-O-B bond [32]. Figure 6 demonstrates that also this fast local motion appears in the anelastic and dielectric spectra at sufficiently low temperature [12]. In fact, around 30 K there is a peak, labelled P_t , in the dielectric and elastic losses measured at frequencies of kHz, whose temperature sensibly increases when D_2O is used for hydration instead of H_2O . If the relaxation rate τ^{-1} associated with this peak were of the overbarrier Arrhenius type, a change of the mass of the hopping ion by a factor of 2 would produce a decrease of τ^{-1} of $\sqrt{2}$, with a less significant shift in temperature. The peak P_d at higher temperature is insensitive to the H mass and is visible in the dielectric but not in the anelastic spectrum, and therefore must be associated with a defect having electric dipole but almost null strain anisotropy, most likely a polaron.

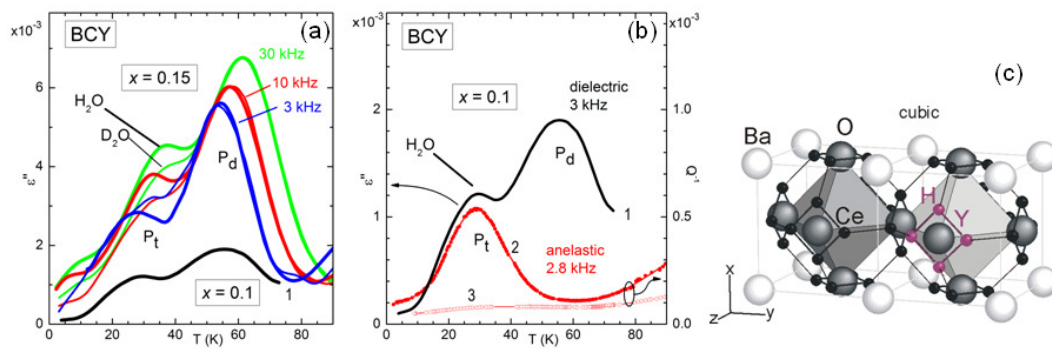


Figure 6. (a) Imaginary dielectric constant of hydrated BCY with $x = 0.1, 0.15$ at LHe temperatures. When D is used instead of H, the dielectric loss presents a marked change in the position of the peak P_t , which is also observed in the anelastic spectrum (b); and therefore is identified with H/D tunneling (data from Ref. [12]); (b) Imaginary dielectric constant (same curve 1 as in (a)) and elastic energy loss Q^{-1} (curve 2) of hydrated BCY with $x = 0.1$; curve 3 is the outgassed state; (c) Two cubic cells of BCY with the positions occupied by H/D as small black spheres. At LHe temperature H is confined and tunnels around an O atom neighbour to the acceptor impurity Y. Adapted with permission from Ref. [12], copyrighted by the American Physical Society.

The complexity of the microscopic processes involved in the ionic mobility and aggregation of perovskites that are highly doped and with tilted octahedra is manifest from the complex anelastic and dielectric spectra, with many features still to be explained, but even those features that seem to have an explanation have in fact unclear points. For example, the intensity of the dielectric relaxation peak due to H/D tunneling is only 3% of the value estimated from the content of H/D and the geometric model in Figure 6 [12], and something similar had been observed in $\text{BaCe}_{1-x}\text{Nd}_x\text{O}_3$ [33]. A possible explanation may be found in the tilting of the octahedra in the low temperature $Pnma$ phase, not shown in Figure 6c, which makes the four positions around the same O atom highly inequivalent, inhibiting tunneling. Then tunneling would occur only in symmetric situations such as within the twin walls between tilted domains, which occupy only a small fraction of the bulk [12].

4. Structural Transformations: Octahedral Tilting in Ionic Conductors

The fact that SrTiO_3 remains cubic down to 105 K and few other perovskites like BaZrO_3 remain cubic even down to the lowest attainable temperatures is the exception rather than the rule. In fact, practically all perovskites of the $\text{A}^{2+}\text{B}^{4+}\text{O}_3^{2-}$ type undergo one or several octahedral tilting transitions during cooling. The reason is that the B-O bonds are shorter and share more charge than the A-O bonds, which therefore are weaker and more anharmonic. As a consequence, during cooling the A-O bonds shorten more than the B-O and at a certain point will create a pressure on the more rigid and incompressible BO_6 octahedra, which therefore tilt (Figure 7).

The tilt patterns are generally indicated in Glazer's notation [34]; for example, the pattern in the low-temperature $Pnma$ orthorhombic phase of BaCeO_3 is $a^+b^-b^-$, meaning that there is a rotation about the a axis with all the octahedra in phase along the axis, and a rotation by a different angle about the b and c axes, with the angles alternately positive and negative along these axes. The series of tilt transition occurring in BaCeO_3 during cooling has been determined from neutron diffraction [35], and it is likely that the same sequence occurs in doped BaCeO_3 , so that the two transitions in Figure 5 are identified as follows: $Pnma (a^+b^-b^-) \xrightarrow{\text{PT1}} Imma (a^0b^-b^-) \xrightarrow{\text{PT2}} R\bar{3}c (a^-a^-a^-) \xrightarrow{\text{PT3}} Pm\bar{3}m (a^0a^0a^0)$, where PT3 is at 1200 K for BaCeO_3 [28,35].

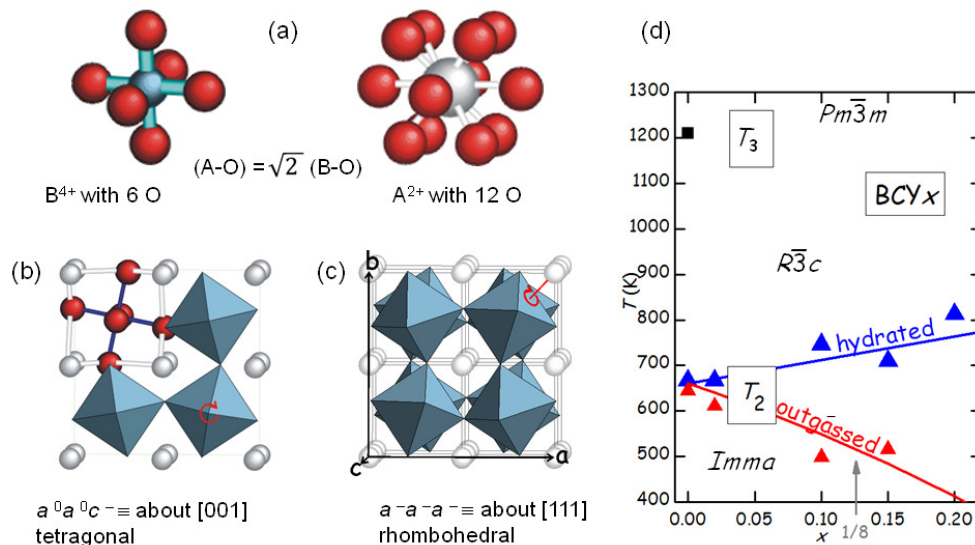


Figure 7. (a) BO_6 octahedra and AO_{12} polyhedra in a cubic perovskite. During cooling, the more rigid and incompressible octahedra tilt in order to fit in the more anharmonic A-O framework. The tilt pattern in (b) is that of SrTiO_3 below 105 K, while that in (c) is for the rhombohedral phase of BCY or the ferroelectric phase of Zr-rich PZT. (d) Temperatures T_2 of the transition PT2 versus Y doping in the outgassed and hydrated states of BCY; T_3 is the temperature of PT3.

The occurrence of structural phase transitions in materials for fuel cells or other applications like gas purification membranes is generally unwanted, because it negatively affects the ionic mobility by reducing and making anisotropic the diffusion coefficients and cause fatigue and cracking of the material under repeated thermal cycles. It is therefore important to study the effect of dopants on the structural transitions, in order to suppress or shift them to safer temperatures, or reduce the magnitudes of the structural changes and therefore the impact on the mechanical stability. Figure 5b shows that the level of O deficiency changes the temperature of PT2 of as much as 250 K on the same sample. It is found that the temperature T_2 of the transition between rhombohedral and orthorhombic structures, occurring with a loss of a tilt axis but increase of the tilt angle about the other two axes [35], increases with the Y substitution x in the hydrated state, but decreases more in the outgassed state. The increase of T_2 with x in the hydrated state is understandable in terms of the larger ionic radius of Y^{3+} with respect to Ce^{4+} , so that the larger YO_6 octahedra have a stronger tendency to tilt and the tilting transition temperature is enhanced. A quantitative measure of the tendency to tilt is the so-called tolerance factor [7]

$$t = \frac{r_A + r_O}{\sqrt{2}(\langle r_B \rangle + r_O)} \quad (6)$$

where r_X is the ideal radius of the ion X, tabulated by Shannon [36], so that $r_A + r_O$ is the ideal Ba-O bond length and $\langle r_B \rangle + r_O$ the ideal B-O bond length averaged over the composition Ce/Y; with this definition, it is $t = 1$ when the ideal bond lengths match exactly those in the cubic cell, while $t < 1$ implies a tendency to tilting. Then the temperature of the n -th tilt transition in the hydrated state can be phenomenologically expressed as [28] $T_n(x) = \Delta T_n [t_n - t(x)]$, where $t(x)$ is calculated with the Shannon radii and is little affected by the fact that the radius of the $(\text{OH})^-$ ion is larger than that of O^{2-} , since it appears in the numerator and denominator; t_n is the critical value of t below which the n -th transition takes place, and ΔT_n is the proportionality factor for the transition temperature. The line passing through the $T_2(x, \delta = 0)$ points in Figure 7d has $\Delta T_2 = 44,300$ K and $t_2 = 0.9577$.

The explanation of the reduction of T_2 after outgassing is based on the fact that the V_O interrupt and, hence, weaken the B-O and A-O networks, so that the above expression of $T_n(x, \delta)$ is reduced by a factor that in a first approximation is assumed to be linear in δ :

$$T_n(x, \delta) = \Delta T_n [t_n - t(x)] (1 - f\delta) \quad (7)$$

The line passing through the $T_2(x, \delta = x/2)$ points of the outgassed state has $f = 5$ [28].

The interplay between V_O and structural transitions is not limited to shifts, however important, in the temperatures of tilt or other types of transitions pre-existing the O loss, but may give rise to ordering transitions of the V_O . These phenomena are usually observed in cobaltites and ferrites, where the mixed valence states of Co and Fe support high levels of O deficiency without further doping, and ordering in the brownmillerite structure occurs at the stoichiometry $ABO_{2.5}$ [37], though more complicated orderings are also found [38]. Since the brownmillerite structure is derived from the perovskite by ordering of the V_O into parallel chains in alternate planes, it is likely that a first stage of V_O ordering consists of chains also in other perovskites [26,39], though its direct observation is very difficult, due to the low cross section of O in TEM and XRD. Other types of V_O ordering may be expected at other commensurate stoichiometries; in Figure 7d a possible anomaly in the behaviour of $T_2(x)$ is marked by an arrow at $x = 1/8$, though measurements at additional compositions would be necessary to confirm this.

Signs of V_O ordering are found also in the anelastic spectra, as demonstrated in Figure 8 by the anomalous increase of the intensity of peak RV with temperature. The three frequencies have been measured during the same run and generally the spectra of BCY are reproducible, without any sign of change of the hydration state, up to 500 K, so that the increase of the height of RV with temperature is significant and in contrast with the usual $1/T$ behaviour. The grey line had been previously measured on the same sample during cooling, and the frequency is higher because the sample had been thinned between the two measurements, but it is closely comparable to the two curves at 3.3 and 18 kHz measured afterwards, and it shows the transition PT1 at 530 K. A possible origin of the anomalous increase of the intensity of RV on approaching PT1 is that some V_O ordering occurs below PT1. We mention that also the other relaxation R6 (see Figure 5), most likely involving V_O , exhibits a similar anomalous behavior, but its close proximity to PT1 makes it likely that also the domain wall motion takes an important role [28].

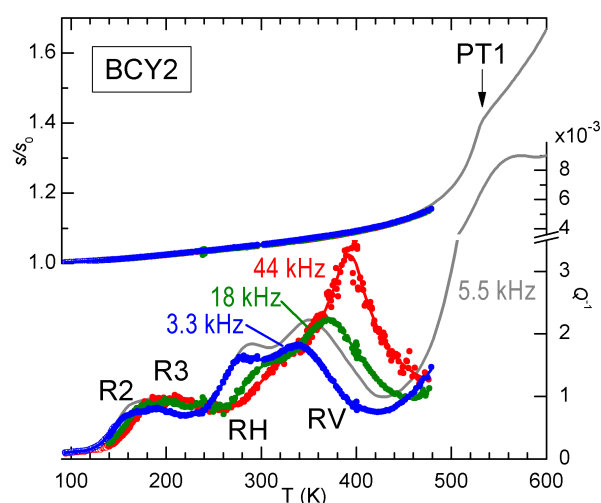


Figure 8. Anelastic spectra of partially hydrated BCY2 measured at three frequencies (data from Ref. [28]).

5. Aging and Recovery of PZT Undergoing FE/AFE Transitions

Ferroelectric (FE) and antiferroelectric (AFE) materials play various roles as materials for energy: through the piezoelectric effect they can be used for mechanical energy harvesting [5], through the electrocaloric effect they can be used for efficient cooling [40], while the peculiar shape of the loop of polarization versus applied electric field exhibited by certain AFE can be exploited for electric energy accumulation with high power density during release [41]. Many of these applications involve repeated FE/AFE transitions, which may be dramatic events on the microscopic scale and cause fatigue and aging. The dielectric spectroscopy is a standard tool for studying FE materials, while the anelastic one is much less, though it can provide a fresh look.

Figure 9 compares the real parts of the elastic compliance s and dielectric constant ϵ of a series of $\text{PbZr}_{1-x}\text{Ti}_x\text{O}_3$ (PZT100 x) samples at various compositions x [42]. The dielectric susceptibility is dominated by the Curie-Weiss peak at T_C , and presents a minor step at T_T , below which tilting of the octahedra with the $a^-a^-a^-$ pattern (see Figure 7) occurs. On the other hand, s presents a step accompanied by a peak at T_C and a step below T_T , which is much less attenuated than in ϵ . This is due to the fact that ϵ probes directly the polarization \mathbf{P} , which is the order parameter of the FE transition, while s probes the strain, which is not directly involved in the FE or tilt transition, but, for symmetry reasons, is only coupled to the square of \mathbf{P} and of the octahedral rotation angles [43]. As a consequence, these transitions produce effects on s that are less dramatic and of comparable strength. The advantage is that it is possible to see also additional effects, such as a new transition at T_{IT} , which had escaped observation for decades, and is interpreted as an initial stage of tilting without long range order [42]. In this manner the tilted region of the phase diagram corresponds to that of low T and low tolerance factor t (see Equation (6), the ionic radius of Zr is larger than that of Ti), without the anomalous depression at $x \simeq 0.06$. In what follows we concentrate on the region of the phase diagram with $x < 0.06$, where the AFE ground state is preceded at higher temperature by the rhombohedral FE phase with disordered tilting. These compositions are of interest for the applications exploiting the AFE/FE transition, such as high energy capacitors and electrocaloric cooling, and we studied the effects of such transition and of aging by means of anelastic spectroscopy.

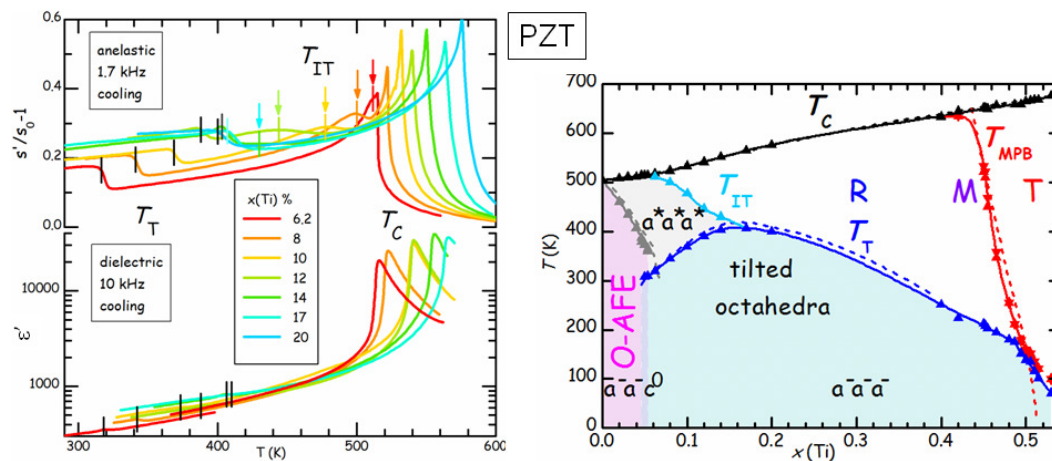


Figure 9. Elastic compliance and dielectric constant of various compositions of PZT. The coloured vertical bars indicated T_C , the arrows T_{IT} and the black arrows T_T , which are plotted in the phase diagram on the right hand side as triangles, together with other compositions. The dashed lines are the generally reported phase diagram of PZT. The ferroelectric phases are R = rhombohedral, T = tetragonal, O-AFE = orthorhombic antiferroelectric. Also indicated are the octahedral tilt patterns (data from Ref. [42]).

We first show in Figure 10 that the elastic anomaly observed at the AFE/FE transition of PZT is far from a simple step, possibly accompanied by a peak, but displays a variety of shapes that change with the heating/cooling rate and state and history of the sample [44,45]. Yet, all the anomalies can be fitted remarkably well with the crude hypothesis that they are the superpositions of steps corresponding to the two tilt modes involved in the transitions around that temperature, namely the $a^-a^-a^-$ mode (labelled T) of the fraction that remains in the rhombohedral (R) FE phase, and the $a^-a^-c^0$ mode of the orthorhombic (O) AFE phase, plus the polar AFE mode. The two anomalies at the tilt transitions consist of steplike softenings on cooling, and hence stiffenings during heating, as observed in Figure 7. Instead, the step of opposite sign, which is clearly visible during all heatings and many coolings, is identified with the polar AFE mode, based on the fact that in the FE phase there is a piezoelectric softening [13], which disappears together with the piezoelectric constants in the AFE phase. Initially we exchanged the assignments of the steps from the OT and AF modes [44,45], because we had not yet recognized the importance of the piezoelectric softening, but those fits are valid with minimal changes in the parameters and exchanging the assignments OT and AF. The curves measured during heating are relatively well reproducible and require limited adjustments in the temperatures and widths of the steps, while those during cooling present much larger variations. From the fits of the PZT5 sample in Figure 10 it appears that an increase of the cooling rate pushes the onset of the AFE transition to lower T , namely increases the thermal hysteresis, whereas tilting in the R-FE phase occurs always promptly at the same temperature and with little thermal hysteresis. In addition, from the variety of the shapes of the $s'(T)$ curves during cooling it appears that the OT tilt and polar AFE modes can be almost independent of each other and occur with slow kinetics over extended temperature ranges in samples subjected to many cycles and aging.

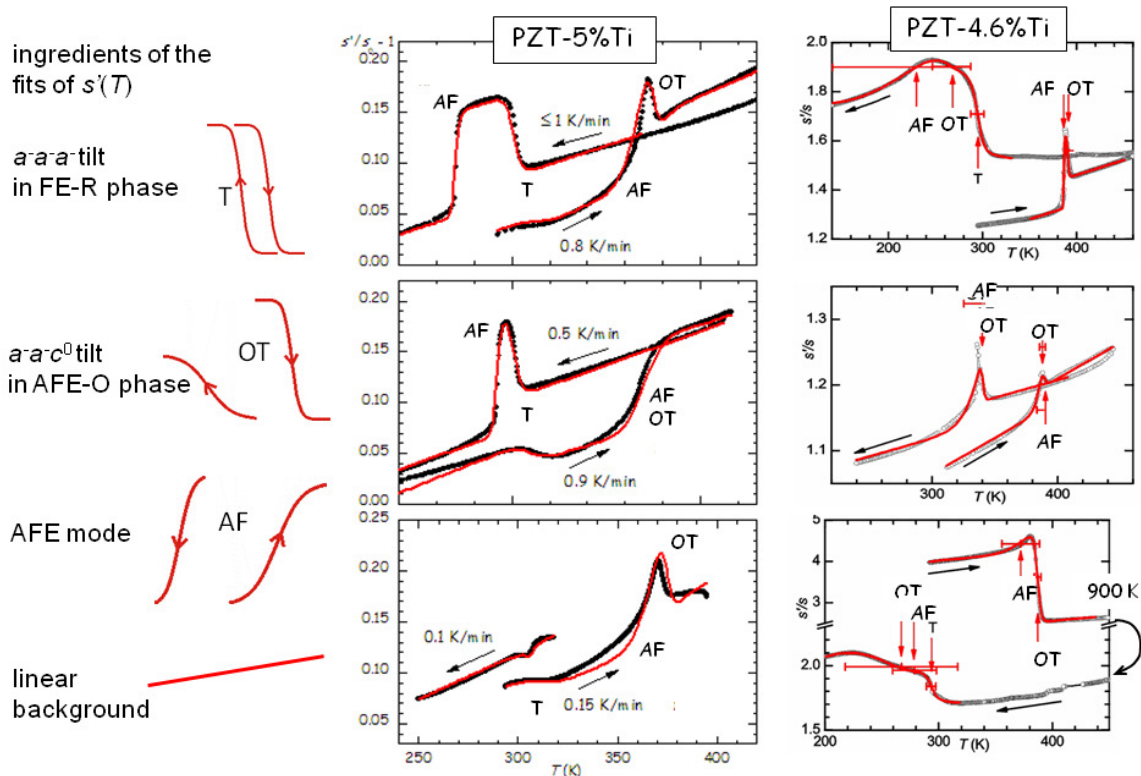


Figure 10. Fits of the elastic anomalies at the AFE/FE transition of PZT with the ingredients indicated on the left. Adapted with permission from Refs. [44,45], copyrighted by the American Physical Society.

The effect of thermal cycling and aging on PZT4.6 is shown in Figure 11, where in the legend are specified the days passed since the first cycle. As already demonstrated in Figure 10, the temperature T_{AF}^h of the AFE/FE transition during heating is stable, though the amplitude of the step is not, while the transition during cooling is much broader and with a large thermal hysteresis. The remarkable fact, however, is the progressive softening of the sample with cycling and aging: it starts from $s \simeq 1.2s_0$ at room temperature and after 25 days it is at $s \simeq 4s_0$, an extraordinarily large softening for a ceramic material whose other properties, e.g., T_C , remain nearly constant. The stiffness can be from partially to more than completely recovered by fast annealing above 600 K. From Figure 11 it appears that extending the measurement to 600 K recovers most of the stiffness, while after reaching 900 K the sample is even stiffer than during the first heating. Though not apparent from Figure 11, after annealing, the transition to the AFE state becomes more prompt, with smaller hysteresis and a narrower shape. These annealing temperatures are rather moderate for this type of ceramic, well below the sintering temperature at which the lattice reconstruction occurs.

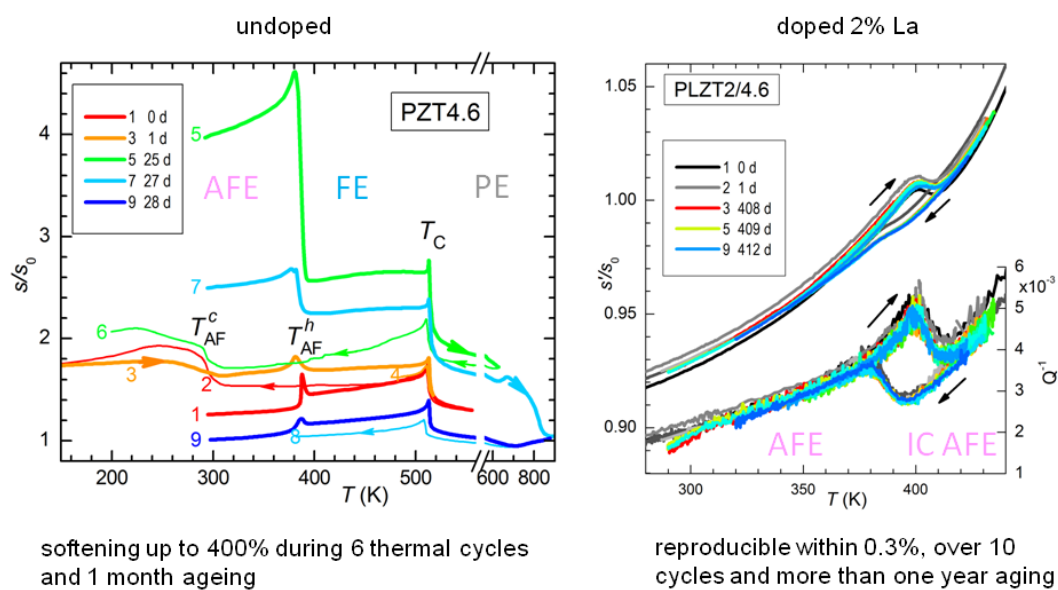


Figure 11. Effect of thermal cycles with AFE/FE transitions, ageing and recovery after high temperature anneal on PZT4.6. By doping with 2% La the FE phase becomes IC AFE and the material becomes perfectly stable under thermal cycles and aging. Adapted with permission from Ref. [46], copyrighted by the American Institute of Physics.

It has yet to be clarified the type of damage created by cycling through the AFE/FE transition and aging and responsible for the huge softening. The most obvious would be cracking, which is known to cause fatigue in these materials, and would be due to the fact that the volume of the AFE cell is markedly smaller than that in the FE phase [47]. Notice however that the measurements are made in vacuum and the rate is 4–8 K/min above 600 K, in order to minimize the O loss. It seems impossible that so mild and fast annealings could heal cracks. Neither can these annealings reoxygenate the material, since the opposite occurs, at least in the surface. We think that the only possibility is that the damage consists mainly of clustering of the V_O created by the PbO loss during sintering. Such a clustering would occur at the charged and stressed walls between AFE and FE domains during the coexistence of the phases at room temperature and during the transitions, as schematically shown in Figure 12a. Then the annealings would dissolve the clusters of V_O and disperse them in the lattice as in the virgin state. It remains to explain how is it possible that concentrations certainly well below 1% of V_O can produce through clustering softening of as much as 4 times, as shown in Figure 11.

In order to verify that the coexistence of AFE and FE phases is responsible for the elastic aging, we tested a sample with the same Ti composition but doped with 2% La on the Pb site. The effect of La is of stabilizing the AFE phase and at the level of 2% even transforms the FE phase into incommensurate (IC) AFE [48], so that the transition is now between two different AFE phases. Therefore, in the La doped sample all the domains have similar volumes and no polarization charge can develop, and indeed the compliance of the doped sample is remarkably stable, within 0.3%, in sharp contrast with the span of over 400% at room temperature in the undoped AFE/FE case (Figure 11).

It is also possible to exclude that the effect of La doping is of neutralizing the V_O . In fact, at high temperature there are various thermally activated anelastic relaxation processes, which also have dielectric counterparts, and most likely are due to the motion of V_O . Figure 12b shows the anelastic spectra of undoped and 2% La-doped PZT4.6 at high temperature, with at least two peaks that are shifted at higher temperature in the spectrum measured at higher frequency. These peaks are relatively stable and appear in practically all the PZT samples we measure. They have the characteristics typical of the motion of highly correlated defects: they are broader than single Debye peaks, Equation (2), have high apparent activation energies (~ 5 eV) with unphysically large relaxation rate extrapolated to infinite T : $\tau_0^{-1} \sim 10^{-35} \text{ s}^{-1}$, which are indicative of relaxation rates that depart from the Arrhenius law, Equation (4) and vanish at finite ordering or freezing temperatures. Since the condition $\omega \sim \tau^{-1}$ holds at the maxima, we think unlikely that the cations can make 10^4 jumps per second around and below 700 K, and the most likely defects involved are V_O . A coherent picture, however, has yet to be found because, if the observation of highly correlated motions seems in accordance with the occurrence of V_O clustering, we have not found clear signs of the dissolution of such hypothetical clusters at high temperature in these relaxation peaks.

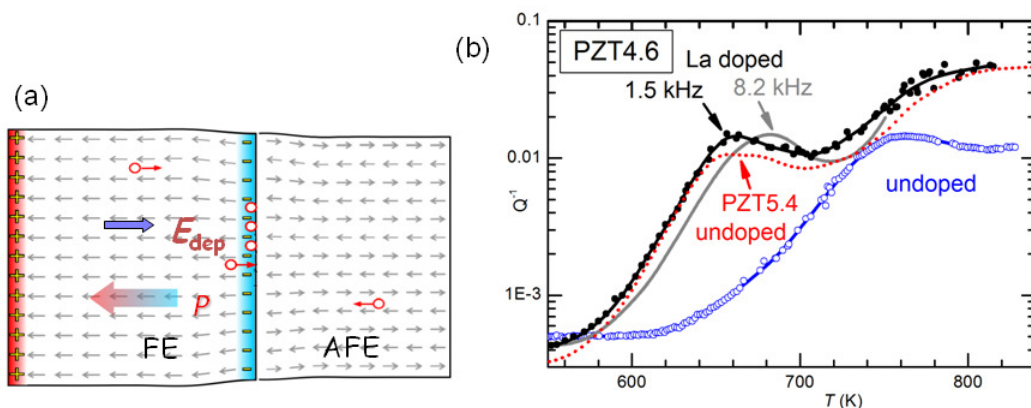


Figure 12. (a) Schematic representation of two neighbouring FE and AFE domains. The gray arrows are the microscopic electric dipoles; the actual AFE pattern in PZT is more complicated. The wall between the two domains is a source of inhomogeneous stress, due to the different cell volumes, and electric field, due to the polarization charge, and for both reasons attracts V_O ; (b) Elastic energy losses of PZT4.6 (empty symbols) PZT4.6 doped with 2% La (closed symbols and continuous line measured at higher frequency) and PZT5.4 (dotted line) (some data from Ref. [46]).

6. Conclusions

We presented a survey of the information that is possible to obtain by anelastic spectroscopy, possibly combined with the dielectric one, on perovskites used as materials for energy conversion and storage. From the anelastic and dielectric spectra measured versus temperature at different frequencies it is possible to analytically study the single steps involved in the ionic migration and clustering, thanks to the fact that each process has a characteristic frequency that, at the temperature at which it matches the measuring angular frequency, produces a peak in the anelastic and dielectric loss. In this manner it is shown that even the diffusion of O vacancies at high dilution, $\ll 1\%$, in the simple cubic

SrTiO₃ is far from the diffusion of dispersed isolated vacancies, but involves pairing and formation of larger complexes, possibly longer chains.

It is clear that a knowledge of this type is necessary for improving the properties of ionic conductors, but the realistic cases of solid electrolytes for fuel cells, highly doped with acceptors in order to be made oxide or proton conductors, are predictably much more complicated than SrTiO₃. From the large amount of information contained in the anelastic and dielectric spectra of such materials only a part can be interpreted in relatively direct manner, and much remains to be done. In any case, the anelastic spectroscopy proves very useful because it provides a cleaner picture than the dielectric spectroscopy of the ionic motions, without the contribution of the electronic conductivity.

In addition to diffusive processes, the anelastic and dielectric spectra, especially the real parts, contain information on phase transitions. The structural phase transitions also have to be studied, since they mechanically damage the material under repeated thermal cycles and can adversely affect the ionic mobilities. The case of BaCe_{1-x}Y_xO₃ is discussed, where several tiltings of the O octahedra occur during cooling from the cubic phase existing at >1200 K. These structural transitions are also connected to the hydration/outgassing level of the material; for example the transition between the rhombohedral and orthorhombic phases can shift by more than 250 K passing from the hydrated to the outgassed state, and a heuristic interpretation of this fact is provided.

Finally, the effect of repeated transitions between the ferroelectric and antiferroelectric states and aging during their coexistence are studied in PZT. Exceptionally large softenings are observed under cycling and aging, which however are fully recoverable after mild annealings. Here also there seems to be a connection with the mobility and clustering of O vacancies at the walls between AFE and FE phases, which are proposed to be at the origin of the observed phenomena.

Acknowledgments: Francesco Cordero thanks P. M. Latino (CNR-ISC) for his technical assistance and improvements in the electronics for the anelastic experiments, and R. Scaccia (CNR-ISC) and A. Morbidini (INAF-IAPS, Roma) for their technical assistance.

Author Contributions: Francesco Cordero, made some anelastic experiments, the outgassing and hydration treatments and wrote the paper. Floriana Craciun made the dielectric experiments and Francesco Trequattrini some anelastic experiments.

Conflicts of Interest: The authors declare no conflict of interest.

References

1. Singhal, S.C.; Kendall, K. *High Temperature Solid Oxide Fuel Cells: Fundamentals, Design and Applications*; Elsevier: Amsterdam, The Netherlands, 2003.
2. Hao, X.; Zhai, J.; Kong, L.B.; Xu, Z. A comprehensive review on the progress of lead zirconate-based antiferroelectric materials. *Prog. Mater. Sci.* **2014**, *63*, 1–57.
3. Chauhan, A.; Patel, S.; Vaish, R.; Bowen, C.R. Anti-ferroelectric ceramics for high energy density capacitors. *Materials* **2015**, *8*, 8009–8031.
4. Valant, M. Electrocaloric materials for future solid-state refrigeration technologies. *Prog. Mater. Sci.* **2012**, *57*, 980–1009.
5. Kong, L.B.; Li, T.; Hng, H.H.; Boey, F.; Zhang, T.; Li, S. *Waste Energy Harvesting Mechanical and Thermal Energies*; Springer: Berlin, Germany, 2014.
6. Li, M.; Pietrowski, M.J.; de Souza, R.; Zhang, H.; Reaney, I.M.; Cook, S.N.; Kilner, J.A.; Sinclair, D.C. A family of oxide ion conductors based on the ferroelectric perovskite Na_{0.5}Bi_{0.5}TiO₃. *Nat. Mater.* **2014**, *13*, 31–35.
7. Goodenough, J.B. Electronic and ionic transport properties and other physical aspects of perovskites. *Rep. Prog. Phys.* **2004**, *67*, 1915–1993.
8. Benedek, N.A.; Fennie, C.J. Why are there so few perovskite ferroelectrics? *J. Phys. Chem. C* **2013**, *117*, 13339–13349.
9. Khomskii, D. Classifying multiferroics: Mechanisms and effects. *Physics* **2009**, *2*, doi:10.1103/Physics.2.20.
10. Stambouli, A.B.; Traversa, E. Solid oxide fuel cells SOFCs: A review of an environmentally clean and efficient source of energy. *Renew. Sustain. Energy Rev.* **2002**, *6*, 433–455.

11. Cordero, F.; Franco, A.; Calderone, V.R.; Nanni, P.; Buscaglia, V. Anelastic spectroscopy for studying O vacancies in perovskites. *J. Eur. Ceram. Soc.* **2006**, *26*, 2923–2929.
12. Cordero, F.; Craciun, F.; Deganello, F.; la Parola, V.; Roncari, E.; Sanson, A. Hydrogen tunneling in the perovskite ionic conductor $\text{BaCe}_{1-x}\text{Y}_x\text{O}_{3-\delta}$. *Phys. Rev. B* **2008**, *78*, 054108.
13. Cordero, F.; Craciun, F.; Trequattrini, F.; Galassi, C. Piezoelectric softening in ferroelectrics: Ferroelectric versus antiferroelectric $\text{PbZr}_{1-x}\text{Ti}_x\text{O}_3$. *Phys. Rev. B* **2016**, *93*, 174111.
14. Cordero, F.; Bella, L.D.; Corvasce, F.; Latino, P.M.; Morbidini, A. An insert for anelastic spectroscopy measurements from 80 K to 1100 K. *Meas. Sci. Technol.* **2009**, *20*, 015702.
15. Nowick, A.S.; Berry, B.S. *Anelastic Relaxation in Crystalline Solids*; Academic Press: New York, NY, USA, 1972.
16. Cordero, F.; Cantelli, R.; Corti, M.; Campana, M.; Rigamonti, A. Tilt-wave dynamics of the oxygen octahedra in La_2CuO_4 and Sr-doped La_2CuO_4 from anelastic and ^{139}La NQR relaxation. *Phys. Rev. B* **1999**, *59*, 12078.
17. Cordero, F. Anelastic (dielectric) relaxation of point defects at any concentration, with blocking effects and formation of complexes. *Phys. Rev. B* **1993**, *47*, 7674–7685.
18. Dattagupta, S.; Balakrishnan, R.; Ranganathan, R. Strain ordering in bcc metals and associated anelasticity. *J. Phys. F Met. Phys.* **1982**, *12*, 1345–1362.
19. Brenscheidt, F.; Seidel, D.; Wipf, H. Elastic aftereffect study of the ferroelastic tetragonal-orthorhombic phase transition in $\text{YBa}_2\text{Cu}_3\text{O}_x$. *J. Alloys Compd.* **1994**, *211*, 264–269.
20. Numakura, H.; Ikeda, T.; Koiwa, M.; Imazouzi, A.A. Self-diffusion mechanism in Ni-based L12 type intermetallic compounds. *Philos. Mag. A* **1998**, *77*, 887–909.
21. Hackmann, A.; Kanert, O. Nmr investigation of defect properties in single crystal SrTiO_3 . *Radiat. Effects Defects Solids* **1991**, *119*, 651.
22. Pasierb, P.; Komornicki, S.; Rekas, M. Comparison of the chemical diffusion of undoped and Nb-doped SrTiO_3 . *J. Phys. Chem. Sol.* **1999**, *60*, 1835–1844.
23. Paladino, A.E. Oxidation kinetics of single-crystal SrTiO_3 . *J. Am. Ceram. Soc.* **1965**, *48*, 476–478.
24. Yamaji, A. Oxygen-ion diffusion in single-crystal and polycrystalline SrTiO_3 . *J. Am. Ceram. Soc.* **1975**, *58*, 152–153.
25. Szot, K.; Speier, W.; Carius, R.; Zastrow, U.; Beyer, W. Localized metallic conductivity and self-healing during thermal reduction of SrTiO_3 . *Phys. Rev. Lett.* **2002**, *88*, 075508.
26. Cordero, F. Hopping and clustering of oxygen vacancies in SrTiO_3 by anelastic relaxation. *Phys. Rev. B* **2007**, *76*, 172106.
27. Cannelli, G.; Cantelli, R.; Cordero, F.; Piraccini, N.; Trequattrini, F.; Ferretti, M. Mobility and aggregation of oxygen in $\text{YBa}_2\text{Cu}_3\text{O}_{6+x}$ in the low-concentration limit. *Phys. Rev. B* **1994**, *50*, 16679.
28. Cordero, F.; Trequattrini, F.; Deganello, F.; la Parola, V.; Roncari, E.; Sanson, A. Effect of doping and oxygen vacancies on the octahedral tilt transitions in the BaCeO_3 perovskite. *Phys. Rev. B* **2010**, *82*, 104102.
29. Yamazaki, Y.; Blanc, F.; Okuyama, Y.; Buannic, L.; Lucio-Vega, J.C.; Grey, C.; Haile, S.M. Proton trapping in yttrium-doped barium zirconate. *Nat. Mater.* **2013**, *12*, 647–651.
30. Björketun, M.E.; Sundell, P.G. Wahnström: A density functional investigation. *Phys. Rev. B* **2007**, *76*, 054307.
31. Oikawa, I.; Takamura, H. Correlation among oxygen vacancies, protonic defects, and the acceptor dopant in Sc-doped BaZrO_3 studied by ^{45}Sc nuclear magnetic resonance. *Chem. Mater.* **2015**, *27*, 6660.
32. Matzke, T.; Stimming, U.; Karmonik, C.; Soetratmo, M.; Hempelmann, R.; Güthoff, F. Quasielastic thermal neutron scattering experiment on the proton conductor $\text{SrCe}_{0.95}\text{Yb}_{0.05}\text{H}_{0.02}\text{O}_{2.985}$. *Solid State Ion.* **2015**, *621*, 86–88.
33. Kuskovsky, I.; Lim, B.S.; Nowick, A.S. Low-temperature dielectric relaxation peaks involving proton tunneling in $\text{Ba}_{1-x}\text{Nd}_x\text{CeO}_3$. *Phys. Rev. B* **1999**, *60*, R3713.
34. Glazer, A.M. The classification of tilted octahedra in perovskites. *Acta Cryst. B* **1972**, *28*, 3384.
35. Knight, K.S. Structural phase transitions, oxygen vacancy ordering and protonation in doped BaCeO_3 : Results from time-of-flight neutron powder diffraction investigations. *Solid State Ion.* **2001**, *145*, 275–294.
36. Shannon, R.D. Revised effective ionic radii and systematic studies of interatomic distances in halides and chalcogenides. *Acta Cryst. A* **1976**, *32*, 751–767.
37. De la Calle, C.; Aguadero, A.; Alonso, J.A.; Fernández-Díaz, M.T. Correlation between reconstructive phase transitions and transport properties from $\text{SrCoO}_{2.5}$ brownmillerite: A neutron diffraction study. *Solid State Sci.* **2008**, *10*, 1924–1935.

38. Clemens, O.; Gröting, M.; Witte, R.; Perez-Mato, J.M.; Loho, C.; Berry, F.J.; Kruk, R.; Knight, K.S.; Wright, A.J.; Hahn, H.; et al. Crystallographic and magnetic structure of the perovskite-type compound $\text{BaFeO}_{2.5}$: Unrivaled complexity in oxygen vacancy ordering. *Inorg. Chem.* **2014**, *53*, 5911–5921.
39. Scott, J.F.; Dawber, M. Oxygen-vacancy ordering as a fatigue mechanism in perovskite ferroelectrics. *Appl. Phys. Lett.* **2000**, *76*, 3801–3803.
40. Lu, S.G.; Zhang, Q. Electrocaloric materials for solid-state refrigeration. *Adv. Mater.* **2009**, *21*, 1983–1987.
41. Hao, X. A review on the dielectric materials for high energy-storage application. *J. Adv. Dielect.* **2013**, *3*, 1330001.
42. Cordero, F.; Trequattrini, F.; Craciun, F.; Galassi, C. Merging of the polar and tilt instability lines near the respective morphotropic phase boundaries of $\text{PbZr}_{1-x}\text{Ti}_x\text{O}_3$. *Phys. Rev. B* **2013**, *87*, 094108.
43. Cordero, F.; Langhammer, H.T.; Müller, T.; Buscaglia, V.; Nanni, P. Rotational instability of the electric polarization and divergence of the shear elastic compliance. *Phys. Rev. B* **2016**, *93*, 064111.
44. Cordero, F.; Craciun, F.; Trequattrini, F.; Galassi, C.; Thomas, P.A.; Keeble, D.S.; Glazer, A.M. Splitting of the transition to the antiferroelectric state in $\text{PbZr}_{0.95}\text{Ti}_{0.05}\text{O}_3$ into polar and antiferrodistortive components. *Phys. Rev. B* **2013**, *88*, 094107.
45. Cordero, F.; Trequattrini, F.; Craciun, F.; Galassi, C. Effects of aging and annealing on the polar and antiferrodistortive components of the antiferroelectric transition in $\text{PbZr}_{1-x}\text{Ti}_x\text{O}_3$. *Phys. Rev. B* **2014**, *89*, 214102.
46. Cordero, F.; Craciun, F.; Trequattrini, F.; Galizia, P.; Galassi, C. Elastic aging from coexistence and transformations of ferroelectric and antiferroelectric states in PZT. *J. Appl. Phys.* **2016**, *120*, 064104.
47. Pokharel, B.P.; Pandey, D. Irreversibility of the antiferroelectric to ferroelectric phase transition in $(\text{Pb}_{0.90}\text{Ba}_{0.10})\text{ZrO}_3$ ceramics. *J. Appl. Phys.* **1999**, *86*, 3327–3332.
48. Asada, T.; Koyama, Y. La-induced conversion between the ferroelectric and antiferroelectric incommensurate phases in $\text{Pb}_{1-x}\text{La}_x(\text{Zr}_{1-y}\text{Ti}_y)\text{O}_3$. *Phys. Rev. B* **2004**, *69*, 104108.



© 2017 by the authors; licensee MDPI, Basel, Switzerland. This article is an open access article distributed under the terms and conditions of the Creative Commons Attribution (CC BY) license (<http://creativecommons.org/licenses/by/4.0/>).